Complex magnetic and transport properties in Pr₃MgBi₅: A material with distorted kagome lattice

Xin Han,[1,2] Yong Li,[1,2] Meng Yang ⦿,[1] Shanshan Miao,[1] Dayu Yan,[1,*] and Youguo Shi[1,2,3]

[1]*Beijing National Laboratory for Condensed Matter Physics and Institute of Physics,*
Chinese Academy of Sciences, Beijing 100190, China
[2]*Center of Materials Science and Optoelectronics Engineering,*
University of Chinese Academy of Sciences, Beijing 100190, China
[3]*School of Physical Sciences, University of Chinese Academy of Sciences, Beijing 100190, China*
and Songshan Lake Materials Laboratory, Dongguan, Guangdong 523808, China

Single crystals of Pr₃MgBi₅ were successfully grown and their structural and physical properties were investigated systematically. Pr₃MgBi₅ crystallizes in a hexagonal structure with the space group of $P6_3/mcm$ (No. 193), in which the Pr^{3+} ions form a distorted kagome lattice in the ab plane. Magnetic measurements and specific heat analysis reveal distinct anomalies at around 10.5 K, indicating an antiferromagnetic phase transition. Meanwhile, an obvious magnetic anisotropy and complex magnetic behavior are observed in this compound. The transport properties of Pr₃MgBi₅ are strongly coupled to its magnetism. Specifically, for $H//ab$, a large and positive quasilinear magnetoresistance is observed at $T = 2$ K, accompanied by anomalies at the metamagnetic transition in the magnetization-field curve. Additionally, a pronounced anomalous Hall effect is observed at low temperatures. Our study not only expands the RE_3MBi_5 (RE = rare earth) family but also provides an excellent opportunity to explore unconventional spin structures arising from the interplay between geometrical frustration and long-range Ruderman-Kittel-Kasuya-Yosida (RKKY) interactions.

I. INTRODUCTION

The investigation of properties in geometrically frustrated magnets has been a hot topic for physicists. Geometrical frustration hinders the minimization of magnetic energy and suppresses conventional magnetic order, leading to the emergence of intriguing ground states such as quantum spin liquids and spin ice [1–5]. Most studies on this phenomenon have focused on insulator compounds, where the nearest-neighbor interactions dominate [6–10]. However, in intermetallic compounds, particularly rare-earth compounds, the Ruderman-Kittel-Kasuya-Yosida (RKKY) interactions play a crucial role by extending the magnetic exchange beyond the nearest neighbors. This results in numerous degenerate exchange interactions and allows for the fine tuning of magnetic order [11–15]. The introduction of long-range spin interactions in a geometrically frustrated spin lattice, such as a triangular lattice or kagome lattice, can lead to the observation of novel quantum ground states. Moreover, the presence of conduction electrons provides an opportunity to study the novel transport properties associated with these exotic magnetic properties. For example, CePdAl and YbAgGe, featuring a distorted kagome sublattice comprising trivalent rare-earth ions, exhibit intricate phase diagrams with novel quantum criticality [16–21]. Furthermore, the observation of the kagome spin ice state in HoAgGe [22] and the emergence of the skyrmion state in the frustrated centrosymmetric

triangular-lattice magnet Gd₂PdSi₃ [23] highlight the importance of exploring new frustrated intermetallic compounds.

The RE_3MPn_5 material (RE = rare earth; M = transition metals or Mg; Pn = Bi, Sb) presents a promising system for investigating magnetic frustration in intermetallics. In these materials, the rare-earth ions form a distorted kagome lattice in the ab plane, similar to the rare-earth ions in the REAgGe family. However, there is a distinct variation in the stacking pattern along the c direction between these two families. Previous studies of the RE_3MPn_5 family have primarily focused on the compounds in which M is transition metal elements [24–29]. Moreover, there is a controversy surrounding the valence states of transition elements in this family [27,30], and some magnetic transition elements may interfere with the study of the magnetic properties of the rare-earth ions [29]. Therefore, the alkaline earth compounds RE_3MgPn_5 could provide a better platform for studying frustrated intermetallics. Until now, only the nonmagnetic compound La₃MgBi₅ has been reported [31], and the lack of suitably sized single crystals has hindered the study of its physical properties.

In this work, we successfully grow single crystals of Pr₃MgBi₅, an interesting member of the RE_3MBi_5 family. Pr₃MgBi₅ exhibits significant magnetic anisotropy and undergoes antiferromagnetic ordering below 10.5 K, displaying complex magnetic behavior at low temperatures. The electronic properties of Pr₃MgBi₅ are strongly coupled to its magnetism. Additionally, a large positive quasilinear magnetoresistance and anomalous Hall effect has also been observed in this compound.
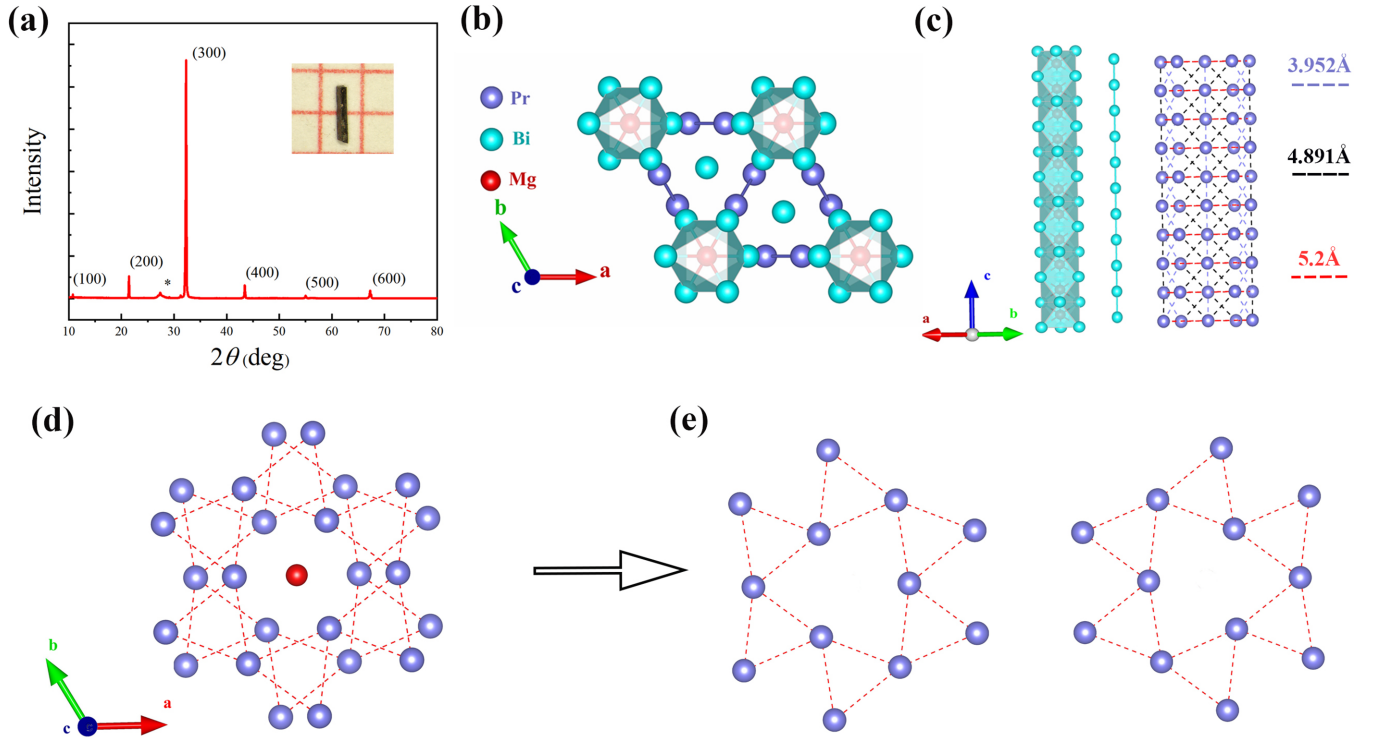
*dayuyan@iphy.ac.cn

124406-1

FIG. 1. (a) X-ray diffraction of a flat surface of Pr_3MgBi_5 single crystals. The inset shows a photograph of Pr_3MgBi_5 single crystals (b) The schematic crystalline structure of Pr_3MgBi_5. (c) Face-sharing $MgBi_6$ octahedra, 1D Bi chains, and Pr sublattice in the structure. (d), (e) Two adjacent distorted kagome layers form by Pr atoms.

II. EXPERIMENTAL DETAILS

Single crystals of Pr_3MgBi_5 were grown by the flux method, following a procedure similar to that employed for growing the nonmagnetic analog, La_3MgBi_5. The raw materials Pr (ingot, 99.9%, Purui Advanced Material Technology Co. Ltd., Beijing, China), Mg (slug, 99.95%, Alfa Aesar), and Bi (pills, 99.999%, Alfa Aesar) were mixed with a mole ratio of 1:6:9 and placed into an alumina crucible. The crucible was then sealed in a quartz tube under high-vacuum conditions. The tube was heated to 1173 K over 10 h and maintained for 24 h. It was then slowly cooled to 993 K at a rate of 2 K/h, followed by centrifuging to separate the crystals from the excess Mg-Bi flux. Rodlike crystals, as shown in the inset of Fig. 1(a), were obtained on the bottom of the crucible.

Single-crystal x-ray diffraction (XRD) was conducted on a Bruker D8 Venture diffractometer at 273 (2) K using Mo $K\alpha$ radiation ($\lambda = 0.71073$ Å). Crystal structure was refined by the full-matrix least-squares method on F^2 using the SHELXL-2018/3 program. The diffraction peaks of the ($h00$) surface for Pr_3MgBi_5 single crystal was obtained via a Bruker D2 phaser XRD detector by using Cu $K\alpha_1$ radiation ($\lambda = 1.54184$ Å). The temperature dependence of magnetic susceptibility $\chi(T)$ was measured in a Magnetic Properties Measurement System (MPMS, Quantum Design) with varied applied fields in the zero-field-cooling (ZFC) and field-cooling (FC) modes. The ac magnetic susceptibility was measured at several frequencies in the MPMS with an excitation field $H = 2$ Oe. Isothermal magnetization M-H was measured on MPMS (7 T) and a Physical Properties Measurement System (PPMS, Quantum Design, 16 T) with a vibrating sample magnetome-

ter (VSM) option. Due to the minimal in-plane anisotropy in magnetization (as shown in Fig. S1 in the Supplemental Material [32]), we no longer specify the exact magnetic-field direction within the ab plane. The electrical transport measurements were performed on the PPMS (9 T) using the standard four-probe technique. The heat capacity (C_P) was measured in the PPMS using its specific heat option with a thermal relaxation method.

III. RESULTS AND DISCUSSION

The single-crystal XRD data reveal that Pr_3MgBi_5 exhibits an anti-Hf_5Sn_3Cu hexagonal structure with space group $P6_3/mcm$ (No. 193) which is also adapted by RE_3MBi_5 family compounds, such as La_3MgBi_5. The refined lattice parameters for Pr_3MgBi_5 were determined to be $a = b = 9.6509$ (2) Å, $c = 6.4852(3)$ Å. These values are smaller compared to the lattice of La_3MgBi_5 [$a = b = 9.7792(2)$ Å, $c = 6.5472(2)$ Å] due to the smaller ionic radius of Pr^{3+}. The detailed crystallographic data and refined atomic positions are summarized in Tables I and II.

The XRD pattern on a flat surface of the Pr_3MgBi_5 single crystal is displayed in Fig. 1(a), where only $h00$ peaks and a low-density peak marked with an asterisk corresponding to the impurity of the Bi flux were detected. The longer dimension of the rodlike samples is along the c axis. Figures 1(b)–1(e) present schematic drawings of the crystal structure for Pr_3MgBi_5. The crystal structure can be described as one-dimensional (1D) chains of Bi and face-sharing $MgBi_6$ octahedra extending along the c directions, and the Pr atoms form a distorted hexagonal substructure. Figure 1(d) depicts

TABLE I. Crystallographic and structure refinement data for Pr_3MgBi_5.

Empirical formula	Pr_3MgBi_5
Formula weight (g mol^{-1})	1491.95
Temperature	273(2) K
Wavelength	Mo $K\alpha$ (0.71073 Å)
Crystal system	Hexagonal
Space group	$P6_3/mcm$ (193)
Unit-cell dimensions (Å)	$a = b = 9.6509(2)$, $c = 6.4852(3)$
Cell volume (Å^3)	523.11(3)
Z	2
Density, calculated (g cm^{-3})	9.472
hkl range	$-15 \leqslant h \leqslant 14$, $-15 \leqslant k \leqslant 14$, $-10 \leqslant l \leqslant 10$
$2\theta_{min}$ (deg), $2\theta_{max}$ (deg)	2.44, 34.01
Linear absorption coeff. (mm^{-1})	97.444
Absorption correction	Multiscan
No. of reflections	16100
No. of independent reflections	420
No. observed reflections	399 [$I > 2\sigma(I)$]
F (000)	1208
R indices	1.82% ($R_1[F_o > 4\sigma(F_o)]$), 3.72% (wR_2)
Weighting scheme	$w = 1/[s^2(F_o^2) + (0.0197P)^2 + 3.3188P]$, where $P = (F_o^2 + 2F_c^2)/3$
Refinement software	SHELXL-2018/3

the arrangement of Pr atoms, with centered Mg atoms, as observed along the c axis. In the ab plane, Pr atoms occupy one crystallographic position and constitute triangular nets. Furthermore, the Pr triangles form a distorted kagome lattice parallel to the ab plane, as shown in Fig. 1(e). These distorted kagome lattices are stacked and symmetrically related by a crystallographic 6_3 screw axis that passes through the Mg atoms along the c direction. This implies that the adjacent kagome layer is rotated by 180° around the c axis. The nearest distance between Pr atoms in kagome plane is 5.2 Å, which is larger than the distance (3.952 and 4.891 Å) between Pr atoms in adjacent layers. In this structure, if we consider the long-range RKKY interaction between Pr^{3+} spins on a frustrated lattice, we can expect a complex magnetic ground state in Pr_3MgBi_5.

Figure 2(a) presents the temperature-dependent magnetic susceptibility $\chi(T)$ measured in the excitation field of 1 kOe for $H//ab$ (χ_{ab}) and $H//c$ (χ_c). We observed a large anisotropy for the low-temperature susceptibility with the ratio of $\chi_{ab}/\chi_c \sim 8$, revealing a pronounced easy-plane anisotropy of

TABLE II. Atomic coordinates and equivalent isotropic thermal parameters of Pr_3MgBi_5 resulting from single-crystal XRD analysis.

Site	WP	x	y	z	U_{eq}	OP
Bi 01	$6g$	−0.26818	0.00000	0.25000	0.004	1
Bi 02	$4b$	0.33333	0.66667	0.50000	0.004	1
Pr 03	$6g$	0.00000	0.38172	0.25000	0.004	1
Mg 04	$2b$	0.00000	0.00000	0.50000	0.002	1

the Pr moments. Figures 2(c)–2(e) show the temperature-dependent χ_{ab} and χ_c at various applied magnetic fields below 30 K. For $H//ab$, $\chi_{ab}(T)$ exhibits a sharp maximum at 10.5 K, indicating an antiferromagnetic transition of $T_N = 10.5$ K. The peak corresponding to T_N shifts to lower temperatures with increasing external field, indicating the antiferromagnetic nature of the magnetic order. Below T_N, there is a significant hysteresis observed between the ZFC and FC curves when 100-Oe magnetic field is applied, suggesting the existence of a small ferromagnetic component. As the applied field increases from 100 Oe to 10 kOe, this irreversibility gets weaker and eventually vanishes. Typically, the irreversibility of magnetic susceptibility is considered a characteristic of spin glass [33]. However, the ac magnetic susceptibility results (as shown in Fig. S2 in the Supplemental Material [32]) rule out this possibility. For $H//c$, the susceptibility shows a small cusp at T_N followed by a slight increase and then a sudden drop at lower temperatures, as shown in Fig. 2(e). Additionally, the $\chi_c(T)$ curve exhibits a broad peak around 60 K, whereas no such anomaly is observed for $H//ab$. This behavior is possibly attributed to the influence of the crystalline electric field (CEF) effect, which has been reported in $CeAgAs_2$ and YbV_6Sn_6 [34,35].

Figure 2(b) presents the temperature dependence of the inverse susceptibility (χ^{-1}) in the 1-kOe field for $H//ab$ and $H//c$. For both field orientations, the data above 150 K can be well fitted by the Curie-Weiss formula $\chi = C/(T - T_\theta)$, where C is the Curie constant and T_θ is the Weiss temperature. The effective moments obtained from the fitted value of the Curie constant are 3.77 μ_B for $H//ab$ and 3.84 μ_B for $H//c$, which are close to the Pr^{3+} free ion moment of 3.58 μ_B. The fitted values of T_θ for $H//ab$ and $H//c$ are 4.85 and −99.9 K, respectively. The positive sign of T_θ for $H//ab$ indicates ferromagneticlike magnetic correlations. However, the relatively large magnitude of negative T_θ observed for $H//c$ may be attributed to the effects of CEF [24,36].

The magnetic susceptibility data reveal that Pr_3MgBi_5 holds a noncollinear antiferromagnetic structure in its ab plane. People have studied the magnetic structure of the isostructural compounds of Nd_3TiSb_5 and Ce_3TiSb_5 and found similar magnetic behavior in Nd_3TiSb_5 [25]. In Nd_3TiSb_5, the Nd^{3+} moments form a noncollinear antiferromagnetic structure with the spins rotated by 120° to each other in the Nd triangles, while the nearest Nd^{3+} moments along the c axis are parallel, leading to three zigzag ladders of ferromagnetically coupled Nd sites. Besides, Ce_3TiSb_5 shows sine-wave-like modulated rows of Ce moments along the c direction and exhibits complex antiferromagnetic behavior in the ab plane, but the nearest neighbors of the Ce moments are also ferromagnetically coupled. For Pr_3MgBi_5, a planar, noncollinear antiferromagnetism with a distorted kagome magnetic sublattice may be responsible for its antiferromagnetic transition at 10.5 K, while the small ferromagnetic component may come from the ferromagnetic coupling between the nearest Pr^{3+} moments. In addition, the low-T magnetic susceptibility for $H//ab$ extrapolates to a finite value at $T = 0$ K, which hints that the magnetic structure is a noncollinear antiferromagnetic type. When $H//c$, the T_N correspondence to the cusp is almost constant as a function of the applied field. Below the T_N, the susceptibility χ_c exhibits
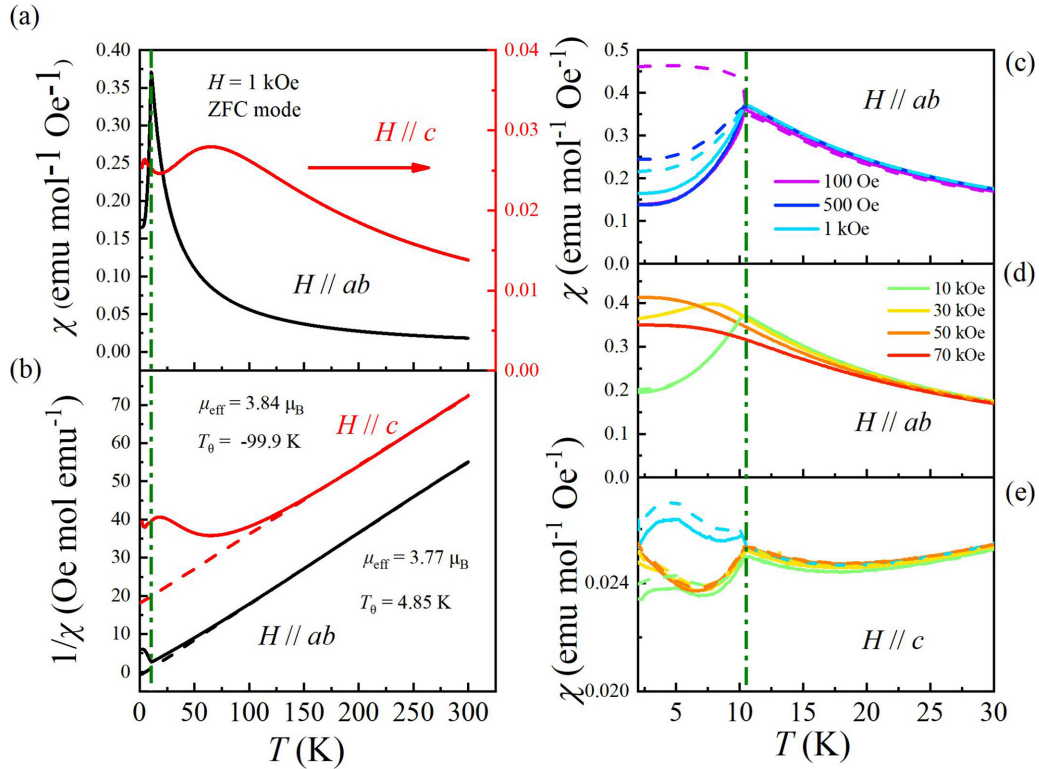
FIG. 2. (a) Magnetic susceptibility χ vs temperature T collected in a magnetic field of $H = 1$ kOe applied parallel to the ab plane and c axis. (b) χ^{-1} vs T for H parallel to the ab plane and c axis. The straight dotted lines are fit to the data using the Curie-Weiss expression as described in the text. (c)–(e) Temperature dependence of the magnetic susceptibility at various applied magnetic fields. (The solid line corresponds to the data of the ZFC mode, while the dashed line corresponds to the FC mode).

complex behavior as the field increases. This also indicates the intricate magnetic structure in Pr_3MgBi_5. Further experimental confirmation by the neutron-diffraction method is necessary to clarify the magnetic nature of this material.

Figure 3(a) displays the isothermal magnetization $M(H)$ measurements of Pr_3MgBi_5, where the magnetic field is applied in the ab plane as well as along the c axis. At a temperature of $T = 2$ K, consistent with the magnetic susceptibility data presented in Fig. 2, the M-H curve also demonstrates an easy-plane anisotropy. In the case of $H//ab$, a metamagnetic transition is observed at a critical field of $H_{ab2} = 30$ kOe. As

the temperature increases, the metamagnetic transition shifts to lower fields and becomes broader. It is consistent with the behavior of the AFM transition T_N observed in the M-T curve in Fig. 2. For temperatures above 15 K, the magnetization shows an almost linear dependence without the presence of metamagnetic transition. Additionally, at the highest applied field of 16 T (as shown in Fig. S3) [32], the magnetization reaches a value of 1.8 μ_B/Pr^{3+}, which is far below the full moment of free Pr^{3+}, $gJ = 3.2$ μ_B, evidencing the important role of the crystal field in the ground-state multiplet of Pr^{3+}. We performed CEF calculations for Pr_3MgBi_5 (presented later
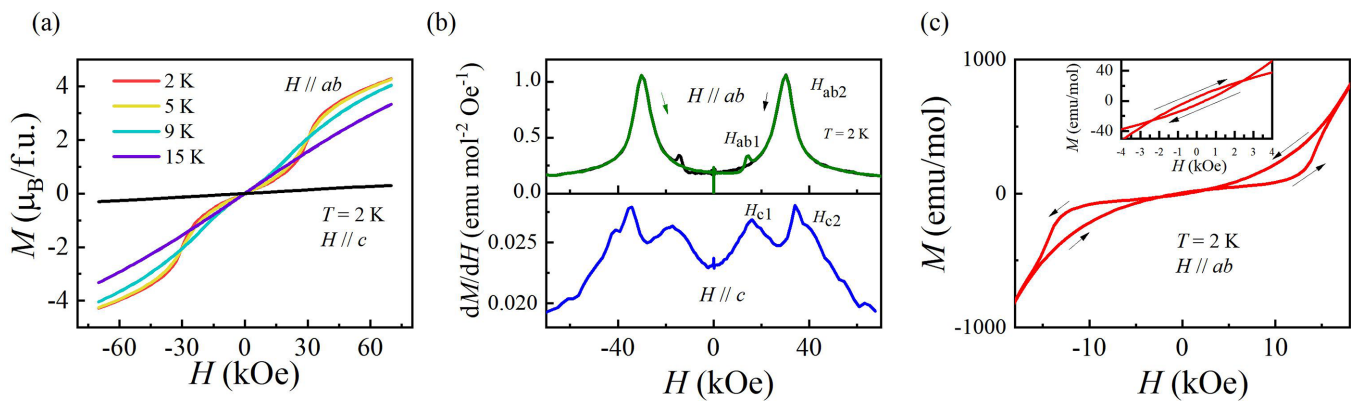

FIG. 3. (a) Isothermal magnetization measured at different temperatures for $H//ab$ and 2 K for $H//c$. (b) dM/dH vs H for both $H//ab$ and $H//c$ at 2 K. (c) The hysteresis in magnetization for $H//ab$ at 2 K obtained by subtracting a paramagnetic background. The inset shows the details in the lower magnetic field.
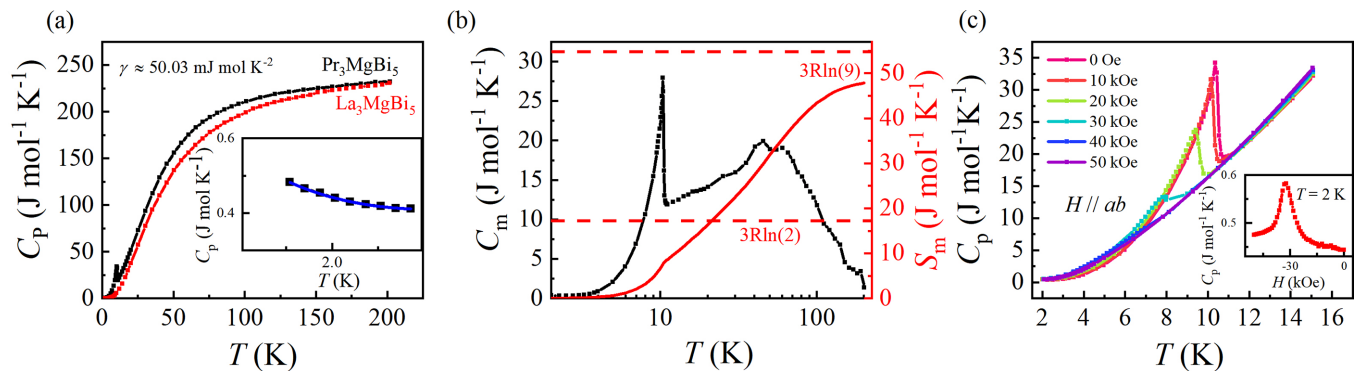
FIG. 4. (a) Temperature dependence of heat capacity of Pr_3MgBi_5 and nonmagnetic La_3MgBi_5. The inset shows the low-temperature part of the heat capacity and the fitting for Pr_3MgBi_5. (b) Temperature dependence of the magnetic specific heat and the corresponding magnetic entropy. (c) Field dependence of the heat capacity. The inset shows the specific heat for $H//ab$ as a function of field.

in this section), revealing that Pr_3MgBi_5 exhibits crystal-field splitting and the Pr^{3+} ion with a total angular momentum quantum number of $J = 4$ splits into nine separate singlet states. Consequently, the magnetic properties of Pr_3MgBi_5 at the lowest temperature are dominated by the pseudodoublet ground state, resulting in the observed reduction in magnetization for the Pr^{3+} ion at 2 K and 16 T. However, one can achieve the saturation value at higher applied magnetic fields. Similar behavior has been observed in many Pr-based intermetallics [37]. Figure 3(b) depicts the first-order derivatives of the *M-H* curve at $T = 2$ K. When the magnetic field is applied parallel to the *ab* plane ($H//ab$), an additional feature is observed at $H_{ab1} = 14.6$ kOe, occurring during the excitation field sweep from 0 to a high field. This corresponds to the hysteresis behavior shown in Fig. 3(c). And we also observed a slight hysteresis near the origin with a remanence as shown in the inset of Fig. 3(c), which is consistent with the divergence of ZFC and FC susceptibility at low fields, suggesting the existence of a small ferromagnetic component in the ordered state. For $H//c$, the d*M*/d*H* curves at $T = 2$ K exhibit two small and broad peaks at $H_{c1} = 17.2$ kOe and $H_{c2} = 34$ kOe in the bottom of Fig. 3(b). These peaks may indicate some weak metamagnetic transitions.

The temperature dependence of the heat capacity for both Pr_3MgBi_5 and the nonmagnetic reference compound La_3MgBi_5 within the temperature range of 1.8–200 K is shown in Fig. 4(a). The bulk nature of the magnetic transitions, as observed in magnetic susceptibility measurements, is confirmed by the λ-shaped peak with appreciable magnitude near 10.5 K in the C_P-T curve. The low-temperature upturn presented in the inset of Fig. 4(a) is likely attributed to a nuclear Schottky effect resulting from the interaction between the nuclear moments and the $4f$ electrons. This phenomenon is commonly observed in other Pr-based compounds [38–40]. For temperatures $T \leqslant 2.5$ K, the heat capacity C_P was fitted to the following expression as done in Refs. [40,41]:

$$C_P = \gamma T + \beta T^3 + (C_N/T^2), \qquad (1)$$

where the first two terms are the electronic and lattice contributions, and the third terms is the contribution from the nuclear Schottky heat capacity due to the splitting of hyperfine levels. The fitting parameters obtained from the fit

are $\gamma = 50.3\,\text{mJ}\,\text{mol}^{-1}\,\text{K}^{-2}$, $\beta = 6\,\text{mJ}\,\text{mol}^{-1}\,\text{K}^{-4}$, and the nuclear Schottky term $C_N = 1.16\,\text{J}\,\text{K}\,\text{mol}^{-1}$. The moderately enhanced value of γ implies the presence of partially hybridized f-electron states, along with only a small enhancement of the effective mass m^* in Pr_3MgBi_5. Besides, the slightly enhanced value of β can be attributed to spin waves in Pr_3MgBi_5, which follow a T^3 dependence in antiferromagnets.

Figure 4(b) presents the temperature-dependent magnetic heat capacity C_m determined by subtracting off the lattice contribution approximated by La_3MgBi_5 and the magnetic entropy S_m calculated by the integral of C_m. As shown in Fig. 4(b), the C_m curve exhibits a shape peak at T_N, confirming the occurrence of a long-range AFM transition, as well as a broad anomaly around 50 K. The broad anomaly corresponds to a Schottky-like effect arising from the thermal variation of the population of CEF levels. The magnetic entropy S_m reaches approximately 50% of $3R\ln2$ at T_N and increases up to $3R\ln2$ by 20 K, where R is the universal gas constant. This behavior suggests a pseudodoublet ground state. In the CEF analysis, the Pr^{3+} ion with a total angular momentum quantum number of $J = 4$ will split into nine separate singlet states [38,42]. However, due to the small splitting energy between the first excited state and the ground state, an admixture of the excited states and the ground state can lead to a pseudodoublet state. This scenario has been used to explain the magnetic ordering of Pr^{3+} ions in many compounds [37,38,43–45]. The reduction of the magnetic entropy at T_N indicates the presence of short-range magnetic fluctuation above T_N. Figure 4(c) shows the magnetic-field dependence of the heat capacity. The λ-shaped peak gradually diminishes and shifts to lower temperatures with increasing magnetic fields, which is consistent with the behavior expected for the AFM transition. The inset in Fig. 4(c) displays the magnetic-field dependence of C_P at $T = 2$ K, where the peak around 30 kOe aligns with the metamagnetic transition observed in *M-H* curves.

The temperature dependence of the electrical resistivity ρ of Pr_3MgBi_5 is shown in Fig. 5(a). When the current is applied along the rod direction (parallel to the c axis), Pr_3MgBi_5 displays metallic behavior with a relatively large residual resistivity ratio $RRR = \rho(300\,\text{K})/\rho(2\,\text{K}) \approx 10.8$. (Because of the limited cross-sectional area in the ab plane of our samples,
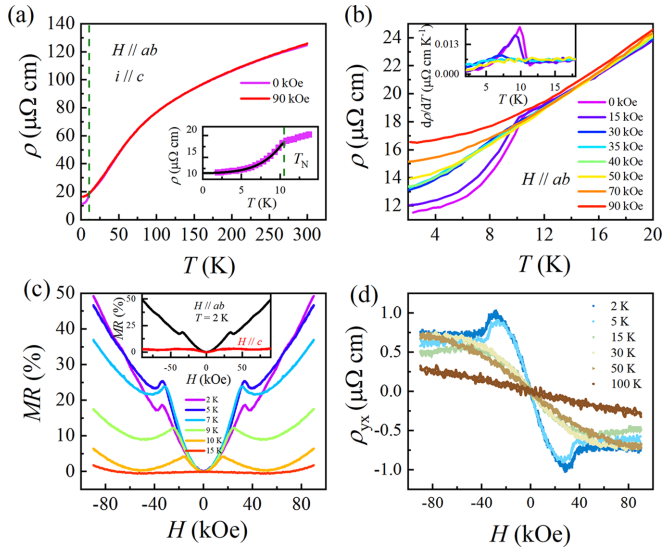
FIG. 5. (a) Temperature dependence of the electrical resistivity at zero field and 90 kOe for $H//ab$. The inset shows the electrical resistivity below the T_N and its fitting. (b) Electrical resistivity below the T_N in different applied fields for $H//ab$. The inset shows the derivative of resistivity. (c) Field dependence of MR in the magnetic field up to 90 kOe for $H//ab$ at various temperatures. Inset: The MR at 2 K for $H//ab$ and $H//c$. (d) The field dependence of Hall resistance at different temperatures.

we were unable to measure the resistivity in the ab plane.) At high temperatures, there is a broad feature centered around 80 K in the resistivity curve, which may be attributed to the thermal depopulation of the CEF levels. At low temperatures and in the absence of a magnetic field, $\rho(T)$ exhibits a sharp decrease below the antiferromagnetic transition temperature (T_N) of 10.5 K. This decrease in resistivity can be attributed to the onset of magnetic ordering in Pr_3MgBi_5, which leads to a reduction in magnetic scattering. Below T_N, the resistivity can be well described by the following expression, as indicated by the black line in the inset of Fig. 5(a):

$$\rho(T) = \rho_0 + AT^2 + B\Delta^5 e^{-\Delta/T}$$
$$\times \left\{ \frac{1}{5}\left(\frac{T}{\Delta}\right)^5 + \left(\frac{T}{\Delta}\right)^4 + \frac{5}{3}\left(\frac{T}{\Delta}\right)^3 \right\}. \quad (2)$$

In this expression, ρ_0 represents residual resistivity, the second term represents the contribution from the Fermi liquid behavior, and the third term arises from the magnon scatting in the antiferromagnet [46,47]. The best fit to the experimental data yields $A = 0.02356\,\mu\Omega\,cm/K^2$, $\rho_0 = 11.416\,\mu\Omega\,cm$, and $\Delta = 11.86$ K. When a magnetic field is applied parallel to the ab plane ($H//ab$), the resistivity below T_N exhibits an increase with increasing magnetic field, eventually reaching a plateau at $H = 90$ kOe, as depicted in Fig. 5(b). The inset of Fig. 5(b) presents the derivative of resistivity below 15 K in different applied fields parallel to the ab plane, where the peak of $d\rho/dT$ shifts to low temperatures as the applied field increases. In the case of a magnetic field applied parallel to the c axis, as shown in the Supplemental Material (Fig. S6) [32], the resistivity of Pr_3MgBi_5 exhibits negligible changes

compared to the resistivity data without a magnetic field. This suggests that the AFM transition is not sensitive to the magnetic field along the c direction, which is similar to the behavior observed in the magnetic measurements.

Figure 5(c) illustrates the magnetic-field dependence of magnetoresistance, $MR = [\rho(H)-\rho(0)]/\rho(0) \times 100\%$, at various temperatures with $H//ab$. Several noteworthy features can be observed in the magnetoresistance data. At a temperature of 2 K, the MR curve exhibits a distinct kink near H_{ab2} after an initial increase. As the temperature is raised to 10 K, the sharp kink in MR becomes broader and shifts to low fields, eventually vanishing at 15 K, which aligns with the behavior of the metamagnetic transition observed in the M-H curves. This correlation between the electronic and magnetic properties of Pr_3MgBi_5 suggests the presence of spin-electron scattering interactions. Furthermore, a significant positive magnetoresistance of up to 50% at 9 T was observed for $T = 2$ K. The MR generally exhibits a decreasing trend with increasing temperature. When the magnetic field is applied above H_{ab2} at 2 K, the MR demonstrates a quasilinear increase without saturation. This behavior cannot be easily explained by conventional Lorenz-force-induced scattering, which typically results in weaker magnetoresistance. Similar large quasilinear positive MR has been observed in HoAgGe and was explained by the presence of uncompensated charge carriers [48]. Moreover, the linear behavior of the MR in the high-field range is commonly observed in Dirac materials, such as $SrMnBi_2$, $YbMnBi_2$, and $EuMnSb_2$ [49–51]. Given the complex magnetism exhibited by Pr_3MgBi_5 and the spin scattering of electrons, further investigations are necessary to fully comprehend the underlying reasons for this magnetoresistance behavior. Additionally, in comparison to the magnetic field applied in the ab plane, the MR for $H//c$ is negligible with fields up to 90 kOe [as depicted in the inset of Fig. 5(c)]. This may suggest that Pr_3MgBi_5 possesses an anisotropic Fermi surface. The anisotropy in the Fermi surface can arise from various factors, such as crystal symmetry, band structure, and spin-orbit coupling, and then lead to variations in the electronic scattering processes and, consequently, different MR behaviors for different field orientations.

In Pr_3MgBi_5, an anomalous Hall effect was observed at low temperatures, as shown in Fig. 5(d). The Hall resistivity (ρ_{yx}) can generally be expressed as the sum of three components: the ordinary Hall effect (ρ_{yx}^N), the anomalous Hall effect coupled to magnetization (ρ_{yx}^A), and the topological Hall effect arising from noncollinear/noncoplanar spin structure (ρ_{yx}^T) [52]. However, in the present study, it was challenging to separate and quantify each individual component accurately. The field-dependent behavior of the anomalous Hall effect observed in Pr_3MgBi_5 is found to be correlated with the field-dependent behavior of magnetization in the M-H curves, indicating a significant interaction between the electrons and local magnetic moments. This interaction can lead to the generation of a Hall voltage perpendicular to the applied electric and magnetic fields, reflecting the influence of the local magnetization on the electron transport properties. At a temperature of 100 K, the observed ρ_{yx} is likely dominated by the ordinary Hall effect, suggesting the
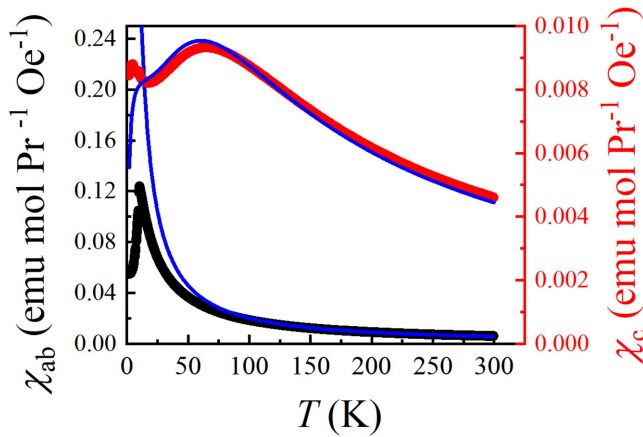
FIG. 6. Temperature dependence of the magnetic susceptibility in Pr_3MgBi_5 when $H = 1$ kOe. The blue line corresponds to the CEF fit.

presence of electron-type carriers with a carrier density of approximately 1.86×10^{22} cm^{-3}. Further investigations and analysis are required to better understand the contributions of each component to the overall Hall resistivity in Pr_3MgBi_5 and to elucidate the underlying physics behind the observed anomalous Hall effect.

In order to further analyze the crystal-field levels and to understand the present anisotropy in the magnetic susceptibility, we have performed a CEF analysis on the susceptibility data. The Pr atoms in Pr_3MgBi_5 occupy the $6g$ Wyckoff position, which has a point symmetry $m2m$ and hence possess orthorhombic site symmetry. This indicates that the $2J + 1$ ground state of the Pr atom splits into nine singlets. To get the energy eigenvalues and the eigenfunctions, we have used the following CEF Hamiltonian to estimate the CEF susceptibility:

$$H_{\mathrm{CEF}} = B_2^0 O_2^0 + B_2^2 O_2^2 + B_4^0 O_4^0 + B_4^2 O_4^2 + B_4^4 O_4^4, \quad (3)$$

where B_l^m and O_l^m are the crystal-field parameters and the Stevens operators [53,54], respectively. The CEF susceptibil-

ity is given by the expression

$$\chi_{\mathrm{CEF}i} = N(g_J \mu_B)^2 \frac{1}{Z} \left(\sum_{m \neq n} |\langle m|J_i|n\rangle|^2 \frac{1 - e^{-\beta m,n}}{\Delta_{m,n}} e^{-\beta E_n} \right.$$

$$\left. + \sum_n |\langle n|J_i|n\rangle|^2 \beta e^{-\beta E_n} \right), \quad (4)$$

where g_J is the Landé g factor; E_n and $|n\rangle$ are the nth eigenvalue and eigenfunction, respectively. J_i ($i = x$, y, and z) is a component of the angular momentum, and $\Delta_{m,m} = E_n - E_m$, $Z = \Sigma_n e^{-\beta E_n}$, and $\beta = 1/k_B T$.

Figure 6 presents the calculated CEF curves as blue lines, which match reasonably well to the experimentally observed data. The anisotropy in the magnetization plots is explained semiquantitatively by the present set of crystal-field parameters. Meanwhile, it nicely reproduces the broad peak around 60 K and the sudden drop around 5 K in the susceptibility when $H//c$. The CEF parameters and the energy levels thus obtained from the diagonalization of the Hamiltonian are given in Table III. A small splitting energy at 3.49 K can be observed between the first excited state and the ground state, corresponding to our magnetic entropy results. The CEF calculations are in good qualitative agreement with the magnetic and specific heat measurements, allowing us to offer a qualitative explanation for the experimental observations. However, for a precise understanding of the crystal-field excitations in this material, future neutron scattering experiments will be necessary.

By extracting the transition temperatures from the magnetization, heat capacity, and resistivity data presented above, a magnetic phase diagram for Pr_3MgBi_5 with the magnetic field parallel to the ab plane can be constructed, as shown in Fig. 7. The phase diagram comprises an AFM ordered phase below 10 K and 30 kOe, and a paramagnetic (PM) phase in other regions. The boundary between the AFM ordered phase and PM phase is determined based on several key observations, including the peaks in the χ-T curves, the metamagnetic transition of H_{ab2} in the M-H curves, the peaks in the C_P-T and C_P-H curves, and the peaks in the derivative of resistivity

TABLE III. CEF fit parameters, energy levels, and wave functions.

CEF parameters				
B_2^0 (K)	B_2^2 (K)	B_4^0 (K)	B_4^2 (K)	B_4^4 (K)
3.3	−0.1	−0.01	0.02	−0.25

| Energy levels					Wave functions				
E (K)	$\lvert-4\rangle$	$\lvert-3\rangle$	$\lvert-2\rangle$	$\lvert-1\rangle$	$\lvert 0\rangle$	$\lvert 1\rangle$	$\lvert 2\rangle$	$\lvert 3\rangle$	$\lvert 4\rangle$
179.00	0.691919	0	−0.00656	0	−0.20594	0	−0.00656	0	0.691919
171.67	0.706084	0	−0.03801	0	0	0	0.038015	0	−0.70608
139.70	0	−0.66288	0	0.246141	0	0.246141	0	−0.66288	0
135.03	0	−0.66969	0	−0.22699	0	0.226986	0	0.669685	0
112.53	−0.03801	0	−0.70608	0	0	0	0.706084	0	0.038015
25.89	−0.04526	0	0.661811	0	−0.34629	0	0.661811	0	−0.04526
20.16	0	0.226986	0	−0.66969	0	0.669685	0	−0.22699	0
3.49	0	−0.24614	0	−0.66288	0	−0.66288	0	−0.24614	0
0.00	0.138562	0	0.248924	0	0.915246	0	0.248924	0	0.138562
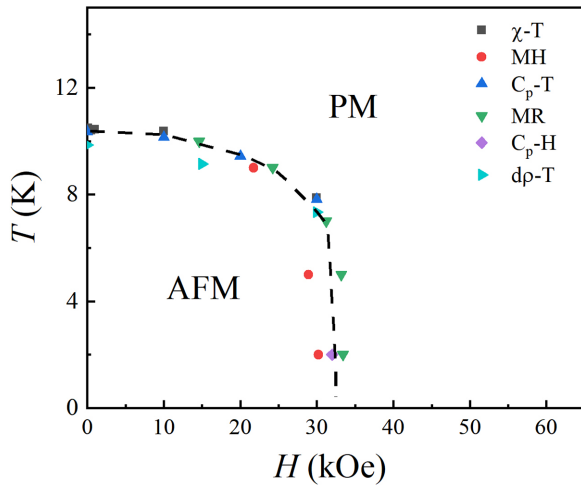
FIG. 7. *H-T* phase diagram of Pr_3MgBi_5 for $H//ab$.

with respect to temperature curves $(d\rho/dT)$, as well as the anomalies in the *MR* curves. These various experimental data collectively suggest the existence of either a field-induced quantum critical point or a quantum phase transition to a saturated paramagnetic behavior. The observed transitions and anomalies in different measurements indicate the complex interplay between magnetic ordering and the influence of the applied magnetic field.

IV. CONCLUSION

In this study, we have investigated the magnetic and electrical properties of Pr_3MgBi_5, an interesting member of $RE_3M Bi_5$ family. Magnetic measurements reveal that Pr_3MgBi_5 exhibits antiferromagnetic ordering at a transition

temperature of $T_N = 10.5$ K, and a metamagnetic transition at $H_{ab2} \sim 30$ kOe from the antiferromagnetic phase to the paramagnetic phase has been observed in *M-H* curves. Meanwhile, Pr_3MgBi_5 shows significant anisotropic magnetic behavior, and the irreversibility of the magnetic susceptibility suggests the presence of a ferromagnetic component, consistent with the observed hysteresis behavior in *M-H* curves. Besides, for the magnetic field applied parallel to the *ab* plane, a sharp kink near H_{ab2} and a nearly linear increase within high magnetic fields in the magnetoresistance are observed at 2 K. Furthermore, a pronounced anomalous Hall effect is detected at low temperatures. The constructed *H-T* phase diagram for the magnetic ordered state of Pr_3MgBi_5 with the magnetic field parallel to the *ab* plane provides insights into the complex magnetic structure of the compound. The observed features suggest the presence of unconventional spin structures in the distorted kagome lattice network of Pr $4f$ moments, and indicate a strong coupling between conduction electrons and Pr^{3+} spins. Further theoretical calculation, neutron-diffraction experiments, and more detailed transport measurements are needed to fully understand the magnetic ground state and electronic behaviors of this unique compound.

[1] J. E. Greedan, Geometrically frustrated magnetic materials, J. Mater. Chem. **11**, 37 (2001).

[2] A. P. Ramirez, Strongly geometrically frustrated magnets, Annu. Rev. Mater. Sci. **24**, 453 (1994).

[3] L. Balents, Spin liquids in frustrated magnets, Nature (London) **464**, 199 (2010).

[4] M. J. Harris, S. T. Bramwell, D. F. McMorrow, T. Zeiske, and K. W. Godfrey, Geometrical frustration in the ferromagnetic pyrochlore $Ho_2Ti_2O_7$, Phys. Rev. Lett. **79**, 2554 (1997).

[5] S. T. Bramwell and M. J. P. Gingras, Spin ice state in frustrated magnetic pyrochlore materials, Science **294**, 1495 (2001).

[6] M. Fu, T. Imai, T.-H. Han, and Y. S. Lee, Evidence for a gapped spin-liquid ground state in a kagome Heisenberg antiferromagnet, Science **350**, 655 (2015).

[7] T.-H. Han, J. S. Helton, S. Chu, D. G. Nocera, J. A. Rodriguez-Rivera, C. Broholm, and Y. S. Lee, Fractionalized excitations in the spin-liquid state of a kagome-lattice antiferromagnet, Nature (London) **492**, 406 (2012).

[8] Y. Okamoto, M. Nohara, H. Aruga-Katori, and H. Takagi, Spin-liquid state in the $S = 1/2$ hyperkagome

antiferromagnet $Na_4Ir_3O_8$, Phys. Rev. Lett. **99**, 137207 (2007).

[9] H. Fukazawa, R. Melko, R. Higashinaka, Y. Maeno, and M. Gingras, Magnetic anisotropy of the spin-ice compound $Dy_2Ti_2O_7$, Phys. Rev. B **65**, 054410 (2002).

[10] H. D. Zhou, C. R. Wiebe, J. A. Janik, L. Balicas, Y. J. Yo, Y. Qiu, J. R. D. Copley, and J. S. Gardner, Dynamic spin ice: $Pr_2Sn_2O_7$, Phys. Rev. Lett. **101**, 227204 (2008).

[11] M. A. Ruderman and C. Kittel, Indirect exchange coupling of nuclear magnetic moments by conduction electrons, Phys. Rev. **96**, 99 (1954).

[12] T. Kasuya, A theory of metallic ferro- and antiferromagnetism on Zener's model, Prog. Theor. Phys. **16**, 45 (1956).

[13] K. Yosida, Magnetic properties of Cu-Mn alloys, Phys. Rev. **106**, 893 (1957).

[14] K.-W. Chen, Y. Lai, Y.-C. Chiu, S. Steven, T. Besara, D. Graf, T. Siegrist, T. E. Albrecht-Schmitt, L. Balicas, and R. E. Baumbach, Possible devil's staircase in the Kondo lattice CeSbSe, Phys. Rev. B **96**, 014421 (2017).

[15] P. Bak, Commensurate phases, incommensurate phases and the devil's staircase, Rep. Prog. Phys. **45**, 587 (1982).

[16] Y. Tokiwa, M. Garst, P. Gegenwart, S. L. Bud'ko, and P. C. Canfield, Quantum bicriticality in the heavy-fermion metamagnet YbAgGe, Phys. Rev. Lett. **111**, 116401 (2013).

[17] S. L. Bud'ko, E. Morosan, and P. C. Canfield, Magnetic field induced non-Fermi-liquid behavior in YbAgGe single crystals, Phys. Rev. B **69**, 014415 (2004).

[18] H. Zhao, J. Zhang, S. Hu, Y. Isikawa, J. Luo, F. Steglich, and P. Sun, Temperature-field phase diagram of geometrically frustrated CePdAl, Phys. Rev. B **94**, 235131 (2016).

[19] S. Lucas, K. Grube, C.-L. Huang, A. Sakai, S. Wunderlich, E. L. Green, J. Wosnitza, V. Fritsch, P. Gegenwart, O. Stockert *et al.*, Entropy evolution in the magnetic phases of partially frustrated CePdAl, Phys. Rev. Lett. **118**, 107204 (2017).

[20] M. Majumder, R. Gupta, H. Luetkens, R. Khasanov, O. Stockert, P. Gegenwart, and V. Fritsch, Spin-liquid signatures in the quantum critical regime of pressurized CePdAl, Phys. Rev. B **105**, L180402 (2022).

[21] H. Zhao, J. Zhang, M. Lyu, S. Bachus, Y. Tokiwa, P. Gegenwart, S. Zhang, J. Cheng, Y. Yang, G. Chen *et al.*, Quantum-critical phase from frustrated magnetism in a strongly correlated metal, Nat. Phys. **15**, 1261 (2019).

[22] K. Zhao, H. Deng, H. Chen, K. A. Ross, V. Petříček, G. Günther, M. Russina, V. Hutanu, and P. Gegenwart, Realization of the kagome spin ice state in a frustrated intermetallic compound, Science **367**, 1218 (2020).

[23] T. Kurumaji, T. Nakajima, M. Hirschberger, A. Kikkawa, Y. Yamasaki, H. Sagayama, H. Nakao, Y. Taguchi, T. Arima, and Y. Tokura, Skyrmion lattice with a giant topological Hall effect in a frustrated triangular-lattice magnet, Science **365**, 914 (2019).

[24] M. Matin, R. Kulkarni, A. Thamizhavel, S. K. Dhar, A. Provino, and P. Manfrinetti, Probing the magnetic ground state of single crystalline Ce_3TiSb_5, J. Phys.: Condens. Matter **29**, 145601 (2017).

[25] C. Ritter, A. K. Pathak, R. Filippone, A. Provino, S. K. Dhar, and P. Manfrinetti, Magnetic ground states of Ce_3TiSb_5, Pr_3TiSb_5 and Nd_3TiSb_5 determined by neutron powder diffraction and magnetic measurements, J. Phys.: Condens. Matter **33**, 245801 (2021).

[26] K. Nakagawa, M. Shinozaki, G. Motoyama, S. Nishigori, K. Fujiwara, M. Manago, and K. Miyoshi, Single crystal growth of Ce_3ZrSb_5 and characterization of the physical properties, in *Proceedings of the 29th International Conference on Low Temperature Physics (LT29)*, Sapporo, Japan (Hybrid), Vol. 38 (Physical Society of Japan, 2023), p. 011083.

[27] J. F. Khoury, B. Han, M. Jovanovic, R. Singha, X. Song, R. Queiroz, N.-P. Ong, and L. M. Schoop, A class of magnetic topological material candidates with hypervalent Bi chains, J. Am. Chem. Soc. **144**, 9785 (2022).

[28] J. F. Khoury, X. Song, and L. M. Schoop, Ln_3MBi_5 ($Ln =$ Pr, Nd, Sm; $M =$ Zr, Hf): Intermetallics with hypervalent bismuth chains, Z. Anorg. Allg. Chem. **648**, e202200123 (2022).

[29] O. Ya. Zelinska and A. Mar, Ternary rare-earth manganese bismuthides: Structures and physical properties of RE_3MnBi_5 ($RE =$ La − Nd) and $Sm_2Mn_3Bi_6$, Inorg. Chem. **47**, 297 (2008).

[30] S. H. D. Moore, L. Deakin, M. J. Ferguson, and A. Mar, Physical properties and bonding in RE_3TiSb_5 ($RE =$ La, Ce, Pr, Nd, Sm), Chem. Mater. **14**, 4867 (2002).

[31] D.-C. Pan, Z.-M. Sun, and J.-G. Mao, Synthesis and crystal structures of La_3MgBi_5 and $LaLiBi_2$, J. Solid State Chem. **179**, 1016 (2006).

[32] See Supplemental Material at http://link.aps.org/supplemental/10.1103/PhysRevMaterials.7.124406 for details of transport properties.

[33] V. H. Tran, F. Steglich, and G. André, Antiferromagnetic order with short correlation length and Kondo interactions in U_2PdGa_3 and U_2PtGa_3, Phys. Rev. B **65**, 134401 (2002).

[34] R. Mondal, R. Bapat, S. K. Dhar, and A. Thamizhavel, Magnetocrystalline anisotropy in the Kondo-lattice compound $CeAgAs_2$, Phys. Rev. B **98**, 115160 (2018).

[35] K. Guo, J. Ye, S. Guan, and S. Jia, Triangular Kondo lattice in YbV_6Sn_6 and its quantum critical behavior in a magnetic field, Phys. Rev. B **107**, 205151 (2023).

[36] A. Maurya, R. Kulkarni, A. Thamizhavel, D. Paudyal, and S. K. Dhar, Kondo lattice and antiferromagnetic behavior in quaternary $CeTAl_4Si_2$ ($T =$ Rh, Ir) single crystals, J. Phys. Soc. Jpn. **85**, 034720 (2016).

[37] Z. Wang, H. Zhao, M. Lyu, J. Xiang, Y. Isikawa, S. Zhang, and P. Sun, Frustrated antiferromagnetism and heavy-fermion-like behavior in $PrPdAl$, Phys. Rev. B **105**, 125113 (2022).

[38] P. K. Das, A. Bhattacharyya, R. Kulkarni, S. K. Dhar, and A. Thamizhavel, Anisotropic magnetic properties and giant magnetocaloric effect in single-crystal PrSi, Phys. Rev. B **89**, 134418 (2014).

[39] S. Królak, H. Świątek, K. Górnicka, M. J. Winiarski, W. Xie, R. J. Cava, and T. Klimczuk, Ferromagnetism in Pr-Rich binary Pr_7Ru_3 intermetallic compound, J. Alloys Compd. **929**, 167279 (2022).

[40] A. K. Pathak, D. Paudyal, Y. Mudryk, K. A. Gschneidner, and V. K. Pecharsky, Anomalous Schottky specific heat and structural distortion in ferromagnetic $PrAl_2$, Phys. Rev. Lett. **110**, 186405 (2013).

[41] S. Sanki, V. Sharma, S. Sasmal, V. Saini, G. Dwari, B. B. Maity, R. Kulkarni, R. Prakash Pandeya, R. Mondal, A. Lakshan *et al.*, Valence fluctuation in $Ce_2Re_3Si_5$ and Ising-type magnetic ordering in $Pr_2Re_3Si_5$ single crystals, Phys. Rev. B **105**, 165134 (2022).

[42] P. Javorsk, H. Mutka, and H. Nakotte, Crystal field in RNiAl compounds studied by inelastic neutron scattering, Appl. Phys. A: Mater. Sci. Process. **74**, s658 (2002).

[43] C. Wang, X. Wang, K. Jia, L. Wang, D. Yan, H. L. Feng, S. Li, and Y. Shi, Single-crystal growth and magnetic anisotropy in $PrFe_2Ga_8$, J. Phys.: Condens. Matter **34**, 165601 (2022).

[44] H. S. Nair, M. O. Ogunbunmi, C. M. N. Kumar, D. T. Adroja, P. Manuel, D. Fortes, J. Taylor, and A. M. Strydom, Pr-magnetism in the quasi-skutterudite compound $PrFe_2Al_8$, J. Phys.: Condens. Matter **29**, 345801 (2017).

[45] M. O. Ogunbunmi, B. M. Sondezi, H. S. Nair, and A. M. Strydom, Electronic and magnetic properties of quasi-skutterudite $PrCo_2Ga_8$ compound, Physica B (Amsterdam) **536**, 128 (2018).

[46] S. Nallamuthu, S. S. Chandrasekaran, P. Murugan, M. Reiffers, and R. Nagalakshmi, Magnetic, thermodynamic and transport properties of novel non-centrosymmetric $RCoSi_3$ ($R =$ Pr, Nd and Sm) compounds, J. Magn. Magn. Mater. **416**, 373 (2016).

[47] X. Zhao, X. Zheng, J. Qi, X. Luo, S. Ma, S. U. Rehman, W. Ren, C. Chen, and Z. Zhong, Anisotropic

magnetocaloric effect and magnetoresistance in antiferromagnetic HoNiGe$_3$ single crystal, Intermetallics **138**, 107307 (2021).

[48] N. Li, Q. Huang, X. Y. Yue, S. K. Guang, K. Xia, Y. Y. Wang, Q. J. Li, X. Zhao, H. D. Zhou, and X. F. Sun, Low-temperature transport properties of the intermetallic compound HoAgGe with a kagome spin-ice state, Phys. Rev. B **106**, 014416 (2022).

[49] L. Zhang, Z. Sun, A. Wang, Y. Xia, X. Mi, L. Zhang, M. He, Y. Chai, T. Wu, R. Wang *et al.*, Strong coupling between magnetic order and band topology in the antiferromagnet EuMnSb$_2$, Phys. Rev. B **104**, 205108 (2021).

[50] A. Wang, I. Zaliznyak, W. Ren, L. Wu, D. Graf, V. O. Garlea, J. B. Warren, E. Bozin, Y. Zhu, and C. Petrovic, Magneto-

transport study of Dirac fermions in YbMnBi$_2$ antiferromagnet, Phys. Rev. B **94**, 165161 (2016).

[51] K. Wang, D. Graf, H. Lei, S. W. Tozer, and C. Petrovic, Quantum transport of two-dimensional Dirac fermions in SrMnBi$_2$, Phys. Rev. B **84**, 220401(R) (2011).

[52] T. Suzuki, R. Chisnell, A. Devarakonda, Y.-T. Liu, W. Feng, D. Xiao, J. W. Lynn, and J. G. Checkelsky, Large anomalous Hall effect in a half-Heusler antiferromagnet, Nat. Phys. **12**, 1119 (2016).

[53] K. W. H. Stevens, Matrix elements and operator equivalents connected with the magnetic properties of rare earth ions, Proc. Phys. Soc., Sect. A **65**, 209 (1952).

[54] P. Fazekas, *Lecture Notes on Electron Correlation and Magnetism* (World Scientific, Singapore, 1999), Vol. 5.